ASTM D5946
ASTM D7334
ASTM D7490
ISO 27448

optical contact angle measurements and drop contour analysis to determine surface energy as well as interfacial and surface tension

force tensiometry, dynamic contact angle measurements, and force of adhesion evaluation

ASTM D1331
ASTM D1417
ISO 1409

ISO/TR 13097

optical turbidity, stability and aging analysis of multi-phase dispersions

zeta potential measurements of fibres, powders, and plate-shaped solids

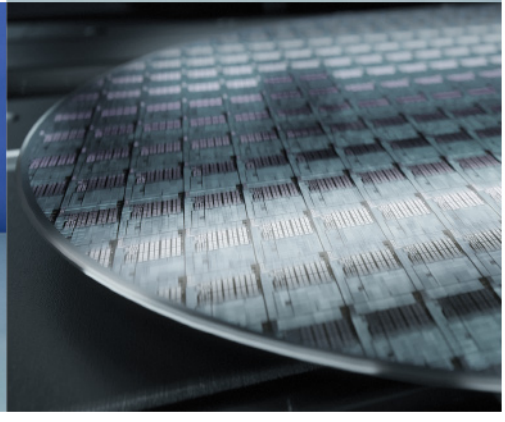

High-end, versatile laboratory measurement device portfolio for a comprehensive analysis of surfaces and interfaces

Learn more >

dataphysics
Understanding Interfaces

DataPhysics Instruments GmbH
Raiffeisenstraße 34 • 70794 Filderstadt, Germany
phone +49 (0)711 770556-0 • fax +49 (0)711 770556-99
sales@dataphysics-instruments.com
www.dataphysics-instruments.com

ADVANCED FUNCTIONAL MATERIALS
www.afm-journal.de

Structural Explanation of the Dielectric Enhancement of Barium Titanate Nanoparticles Grown under Hydrothermal Conditions

Ana F. Suzana, Sizhan Liu, Jiecheng Diao, Longlong Wu, Tadesse A. Assefa, Milinda Abeykoon, Ross Harder, Wonsuk Cha, Emil S. Bozin, and Ian K. Robinson**

When synthesized under certain conditions, barium titanate ($BaTiO_3$, BTO) nanoparticles are found to have the non-thermodynamic cubic structure at room temperature. These particles also have a several-fold enhanced dielectric constant, sometimes exceeding 6000, and are widely used in thin-layer capacitors. A hydrothermal approach is used to synthesize BTO nanocrystals, which are characterized by a range of methods, including X-ray Rietveld refinement and the Williamson–Hall approach, revealing the presence of significant inhomogeneous strain associated with the cubic phase. However, X-ray pair distribution function measurements clearly show the local structure is lower symmetry than cubic. This apparent inconsistency is resolved by examining 3D Bragg coherent diffraction images of selected nanocrystals, which show the existence of ≈50 nm-sized domains, which are interpreted as tetragonal twins, and yet cause the average crystalline structure to appear cubic. The ability of these twin boundaries to migrate under the influence of electric fields explains the dielectric anomaly for the nanocrystalline phase.

1. Introduction

Barium titanate ($BaTiO_3$, BTO) is a perovskite type oxide, presenting five different crystalline structures depending on the temperature: rhombohedral at low temperature, orthorhombic, then tetragonal and becoming cubic above T_C = 120 °C.[1] The cubic structure is stable up to 1460 °C, and above this temperature, a hexagonal phase becomes thermodynamically stable. At room temperature (RT) BTO assumes a tetragonal structure, which guarantees ferroelectricity under ambient conditions, with useful applications as a lead-free ferroelectric material.[2,3] BTO was discovered in 1941,[4] and since then it has been used in the fabrication of devices such as multilayer ceramic capacitors (MLCCs) due to its piezoelectric behavior and the enhanced dielectric properties found in nanoparticles (NPs), with world-wide production exceeding 10^{12} units per year.[5] The detailed understanding of the dielectric enhancement is lacking, and the mechanism is still under investigation. Several methodologies are used in the preparation of metal oxides such as BTO, including solid-state reactions,[6] the sol-gel route,[7] and microwave-guided approach.[8] Of particular interest here is the widely-used hydrothermal synthesis, which is a process for the production of nano- to micron-sized crystals based on the enhancement of the solubility of the initial metal precursors under high-pressure solvent conditions.

BTO nanoparticles are known to have a several-fold enhancement of their dielectric constants, with a maximum value for particles in the size range 140 nm[9] to 1 µm.[5] Models have been

A. F. Suzana,[+] L. Wu, T. A. Assefa,[++] E. S. Bozin, I. K. Robinson
Condensed Matter Physics and Materials Science Division
Brookhaven National Laboratory
Upton, NY 11973, USA
E-mail: asuzana@bnl.gov; irobinson@bnl.gov

The ORCID identification number(s) for the author(s) of this article can be found under https://doi.org/10.1002/adfm.202208012.

[+]Present address: Chemical Sciences and Engineering Division, Argonne National Laboratory, Lemont, IL 60439, USA

[++]Present address: Stanford Institute for Materials and Energy Sciences, Stanford University and SLAC National Accelerator Laboratory, Menlo Park, CA 94025, USA

S. Liu
Energy Storage Division
Interdisciplinary Science Department, Brookhaven National Laboratory
Upton, NY 11973, USA

J. Diao, I. K. Robinson
London Centre for Nanotechnology
University College London
London WC1E 6BT, UK

M. Abeykoon
Photon Sciences Division
Brookhaven National Laboratory
Upton, NY 11973, USA

R. Harder, W. Cha
Advanced Photon Source
Argonne National Laboratory
Lemont, IL 60439, USA

DOI: 10.1002/adfm.202208012

proposed for this enhanced dielectric behavior at small particle size, including core-shell structures,[10] domain wall motion,[11] or internal residual stress in fine-grained BTO.[12,13] Here we provide strong evidence from Bragg Coherent Diffraction Imaging (BCDI) experiments in favor of a model based on field-induced migration of low energy twin boundaries[11,14] between strained nanoscale tetragonal domains arrayed in nanoparticles with average cubic symmetry. Even though the paraelectric cubic phase is not thermodynamically favorable at RT, several research works have reported that nanocrystals adopt a cubic crystalline structure at ambient conditions with or without the coexistence of the expected tetragonal phase.[15–18] This demonstrates that the crystalline structure evolution is complex and very sensitive to the synthesis methodology and conditions. Since the cubic metastable phase at RT is commonly reported for BTO, several explanations have been proposed for its stabilization. One model is that Ba^{2+} vacancies and hydroxyl ions are incorporated into the crystalline lattice.[19] Given the need of a very high pH environment for the hydrothermal synthesis (pH > 12, see below), the incorporation of OH^- into the crystalline structure is common and has been widely reported.[15,19,20] The second model suggests that when the hydrothermal approach is used, the synthesis parameters, such as deviations in the Ba:Ti molar ratio and the synthesis temperature, stabilize the cubic phase.[21,22] The third model is based on the critical size argument, related to the excess surface energy associated with all NPs, where particles below a "critical size" are prompted to have cubic symmetry.[23] This is by analogy to the formation of anatase, rather than rutile for NPs of TiO_2.[24] Here we will argue in favor of a fourth model, in which the cubic phase is stabilized by strain.

Here, we study the nanocrystals obtained by a hydrothermal approach to produce high-quality BTO NPs, using a range of different synthesis conditions: one set of syntheses was done at 180 °C, using different alcohols, and one sample with no alcohol was prepared for comparison purposes. The relatively low temperature is reported to lead to the formation of a mixture of metastable cubic and tetragonal phases at RT.[21] Another sample was prepared using 240 °C as the nominal temperature, and a higher Ba/Ti molar ratio, which is reported to lead predominantly to the formation of the tetragonal symmetry phase. The goal of this investigation was to determine the influence of the hydrothermal synthesis parameters in the formation of the BTO metastable cubic phase, noting that the thermodynamic stable phase is tetragonal. Atomic pair distribution function (PDF) technique and Raman spectroscopy show that the crystalline structure is locally distorted. From the X-ray diffraction (XRD) data the crystalline structure was refined using the Rietveld method, and Williamson–Hall (W–H) plots were prepared for all the samples, from where we determined the crystallite size and inhomogeneous strain (microstrain). These data indicate that the structure is, on average, either fully cubic or there is a mixture cubic+tetragonal at RT, depending on the sample. For comparison, we also investigated a commercial BTO nanocrystal sample, supposed to be fully tetragonal, as a reference. We then used Bragg coherent diffraction imaging (BCDI, see Supporting Information for technique details) to show the presence of phase-shifted domains within the NPs, which can be interpreted as twin domains crossing the particles.

2. Results and Discussion

2.1. Particle Shape and Size

The grain size and morphology of the BTO nanocrystals were investigated first by scanning electron microscopy (SEM). **Figure 1** shows representative images of the five different samples synthesized under hydrothermal conditions, alongside a commercial sample. The samples naming attribution is described in the Experimental Section. From the images one can see that the general morphology is cube-shaped. In perovskite structures, the {100} planes have the lowest surface energy and, therefore, they have the slowest growth rate. The higher energy {111} edges of the cubic-shaped particles grow preferably, and the resulting equilibrium shape of the structure is cubic.[15] From the SEM images one can clearly see that when no alcohol was used, the nanocrystals assume a spherical shape, with a rough surface, in contrast with the sharp terminations seen for the nanocrystals when an alcohol was used in the synthesis procedure, Indicating that the alcohol plays a role in the facet stabilization of the BTO nanocrystals.

2.2. Long-Range Order

Figure 2a displays the XRD patterns for the six samples (see Methods for further details). The inset shows that, when the sample is tetragonal, there is a peak splitting of the (110) into (110) and (101) reflections, separated in reciprocal space, as clearly shown for the commercial sample. There is a similar peak splitting for the {200} set of planes in the cubic structure, that splits into (002) and (200) for the tetragonal phase, shown in Figure S1, Supporting Information. From these plots, it is immediately noticeable that there is a mixture of both tetragonal and cubic phases at RT for the ethanol, no alcohol, and 240 °C samples. To extract the relative composition of the mixture, we performed a Rietveld refinement of the crystalline structure, discussed below.

From the XRD patterns, Rietveld analysis was done for all the BTO NPs. Figure S2, Supporting Information, shows the refinement plots, and **Table 1** summarizes the parameters originating from the crystalline refinement. Several additional peaks can be seen for the sample BTO ethanol, all of them indexed as barium carbonate ($BaCO_3$), a impurity commonly reported in the hydrothermal synthesis of BTO.[17] All the samples presenting $BaCO_3$ were washed with a 3% hydrochloric acid solution, followed by centrifugation, and only Bragg peaks from the BTO phase were seen in a XRD laboratory measurement for these samples after the washing procedure, demonstrating that the acid washing removes the $BaCO_3$. For the commercial sample, the structure is mainly composed of tetragonal phase, with coexistence of cubic phase. A minor concentration of $BaCO_3$ is also present. For the samples butanediol and PG, the structure is fully cubic, and for the samples 240 °C, ethanol, and no alcohol, there is a mixture of both phases. While the crystallite size of the commercial sample is in good agreement with the SEM images, for the samples 240 °C, butanediol, and PG, the size is much smaller, around 25 nm, than shown by the SEM imaging, indicating the presence of disorder in the sample. This observation is central to the conclusions of this paper and leads us to a model explaining the presence of the disorder, based mostly on BCDI results,

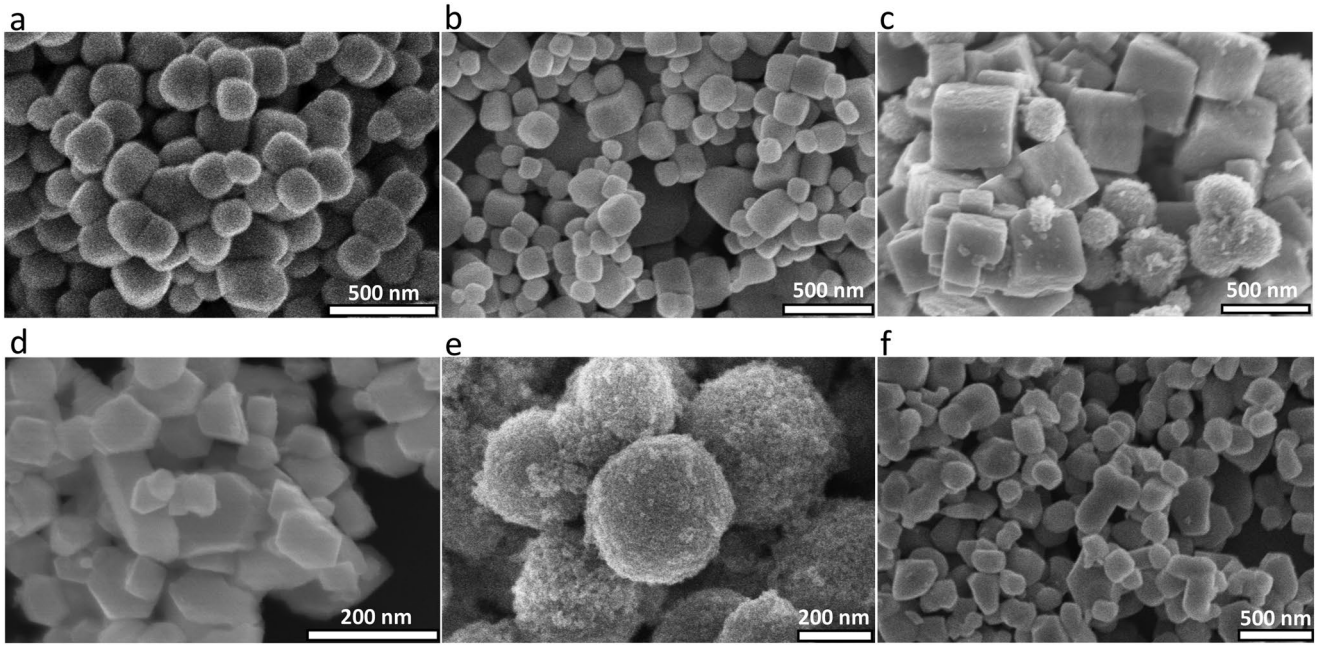

Figure 1. SEM images of the as-synthesized samples using the hydrothermal method. a) BTO ethanol, b) BTO 240 °C, c) BTO NPs synthesized using butanediol, d) using propylene glycol, e) using no alcohol in the synthesis procedure, and f) the commercial BTO sample.

discussed below. The sizes for the ethanol and no alcohol samples are bigger, in the 114–194 nm range. The Rietveld analysis-derived strain for the tetragonal phase of the commercial sample is very small, indicating a conventional crystalline structure. However, the microstrain for the cubic phase component is substantial in all cases. The strain values for the samples synthesized by the hydrothermal method are high, and, when there is a mixture of phases, the strain for the cubic metastable phase was always higher than that of the tetragonal phase. The high microstrain values for the cubic phase could be understood as originating from the presence of twin domain regions within the NPs, as supported by the BCDI analysis below.

2.3. Local Order

The atomic PDF method uses high energy X-rays and probes a broad range of reciprocal space. In our work, PDF data were

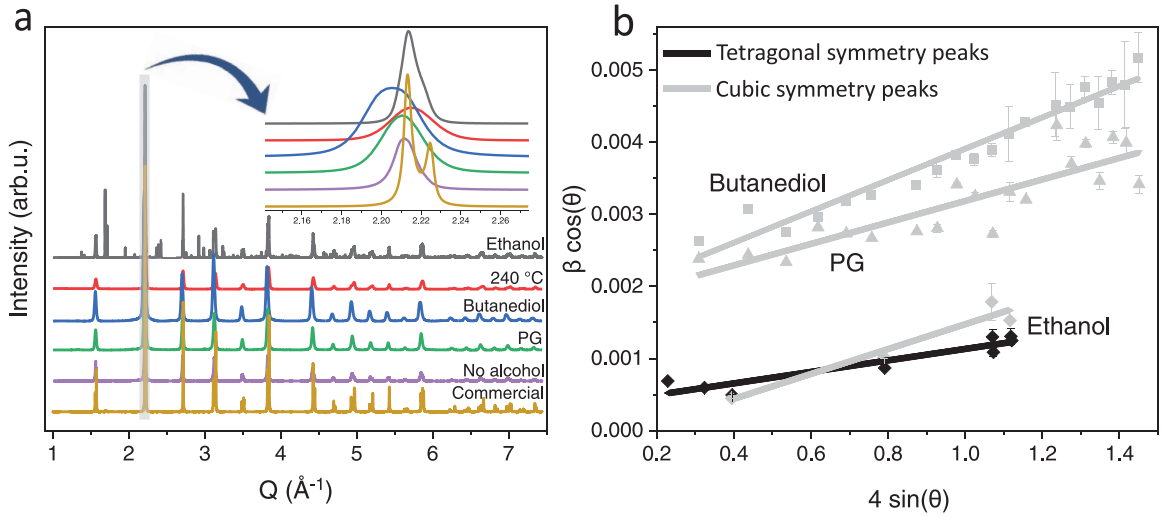

Figure 2. XRD and *W–H* plot of the BTO NPs. a) XRD patterns of the samples synthesized by the hydrothermal approach and the commercial sample (the names of the samples are included in the bottom right side of the plots). The inset enlarges the (110) reflection, that is split into the additional (101) Bragg peak in the case of tetragonal phase. b) Williamson-Hall plots $\beta\cos\theta$ versus 4 $\sin\theta$ for the BTO samples, where β is the FWHM. The straight lines represent the linear fits for each sample. The names of the corresponding samples are indicated. The reflections indexed as cubic phase were plotted separately, shown in gray. The tetragonal symmetry peaks are shown in black.

Table 1. Parameters from the Rietveld refinement for the BTO samples synthesized through hydrothermal approach and the commercial sample. C and T denote cubic and tetragonal phases, respectively.

Sample	Phase composition [%]	Size [nm]	Inhomogeneous strain [%]	Lattice parameters [Å]	R_{wp} [%]
BTO commercial	C:14.1 T: 84.9 $BaCO_3$: 1.0	C: 203.7 T: 32.1	C: 0.64 T: 0.08	C: $a = 4.0088$ T: $a = 3.9944$, $c = 4.0358$	9.83
BTO 240 °C	C: 38.7 T: 61.3	C: 23.4 T: 28.3	C: 0.28 T: 0.26	C: $a = 4.0097$ T: $a = 3.9942$, $c = 4.0305$	3.34
BTO ethanol	C: 31.4 T: 55.1 $BaCO_3$: 13.5	C: 191.7 T: 143.8	C: 0.48 T: 0.28	C: $a = 4.0144$ T: $a = 3.9983$, $c = 4.0309$	9.64
BTO butanediol	C: 100	24.4	0.6	C: $a = 4.0289$	5.74
BTO no alcohol	C: 72.21 T: 26.83 $BaCO_3$: 0.96	C: 194.0 T: 114.4	C: 0.49 T: 0.395	C: $a = 4.0198$ T: $a = 4.0009$, $c = 4.0299$	8.56
BTO PG	C: 100	25.9	0.4859	C: $a = 4.0185$	3.84

collected and processed as described in the Experimental Section, and direct space fits were carried out using cubic and tetragonal models over the 1.2–80 Å range, shown in **Figure 3**a as well as over 1.2–10 Å in Figure 3b using orthorhombic and rhombohedral models as applied for the butanediol sample data. The cubic model gave a worse fit than tetragonal for all samples (Table S1, Supporting Information) over the wide refinement range, with one example shown in Figure 3a. The distortion parameter t for the tetragonal structure was estimated using the definition adopted from Page et al.[25] Additionally, orthorhombic and rhombohedral models were also fit over 1.2–10 Å to account for small apparent splitting of the Ti—O nearest neighbor PDF peak indicative of further symmetry lowering. In some instances (see Table S2, Supporting Information) these fits were giving the smallest fit residuals, suggesting that the underlying local (sub-nanometer) off-centering distortions are likely along [110] or [111] directions, rather than [100], portraying the multiscale complexity of domains akin to that reported in previous PDF work on $BaTiO_3$.[26] Importantly, the observation from PDF that the local structure is of low symmetry, tetragonal or lower, is in stark contrast to the preferentially cubic long-range structure.

Figure 4a shows the Raman spectra for all the BTO NPs. The presence of sharp band at around 305 cm^{-1} indicates asymmetry within the TiO_6 octahedra of BTO and is considered to be a fingerprint of the local structure found in the tetragonal phase.[17,27–29] This band is evident for all the samples studied, albeit with varying amplitude. Specifically, the band is more pronounced for the commercial, 240 °C and ethanol samples, indicating that the main phase present is tetragonal, in agreement with the Rietveld refinements discussed above. Raman spectroscopy is a local probe, and the indication of tetragonal local structure is consistent with the PDF observations. Figure 4b shows the Fourier transform infrared (FTIR) spectroscopy carried out for the BTO powders. Specifically, there is a sharp band at 3500 cm^{-1} for the butanediol, no alcohol and PG samples. This band has been attributed to lattice OH^- trapped in the crystalline structure.[23] Those are precisely the samples

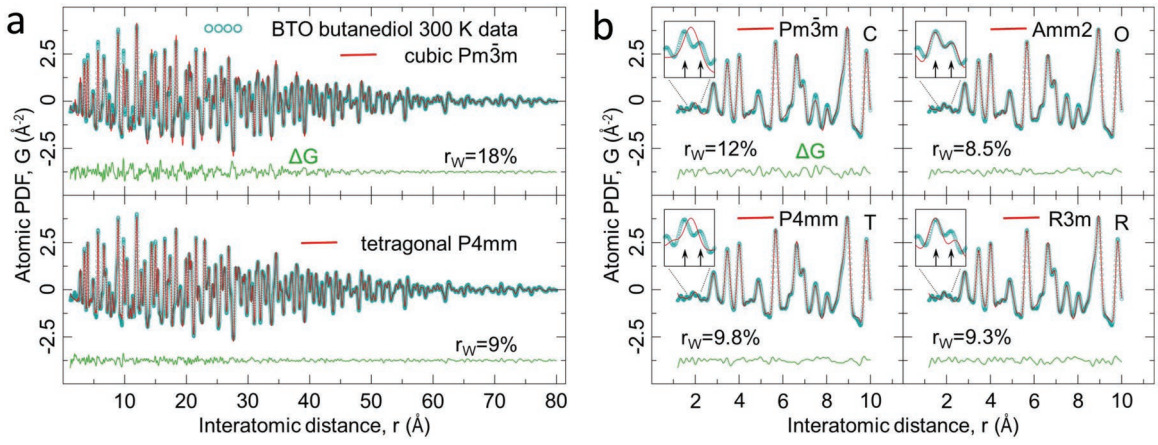

Figure 3. PDF analysis example. a) Pair distribution function $G(r)$, analysis of the BTO-butanediol sample over the 1.2–80 Å range. Fit residuals, r_w, are as indicated. b) Fits for the BTO-butanediol sample data using cubic, tetragonal, orthorhombic, and rhombohedral models over the 1.2–10 Å range. The insets on the top left show PDF features related to Ti—O nearest neighbor octahedral distances in BTO. Vertical ticks mark model-predicted distances.

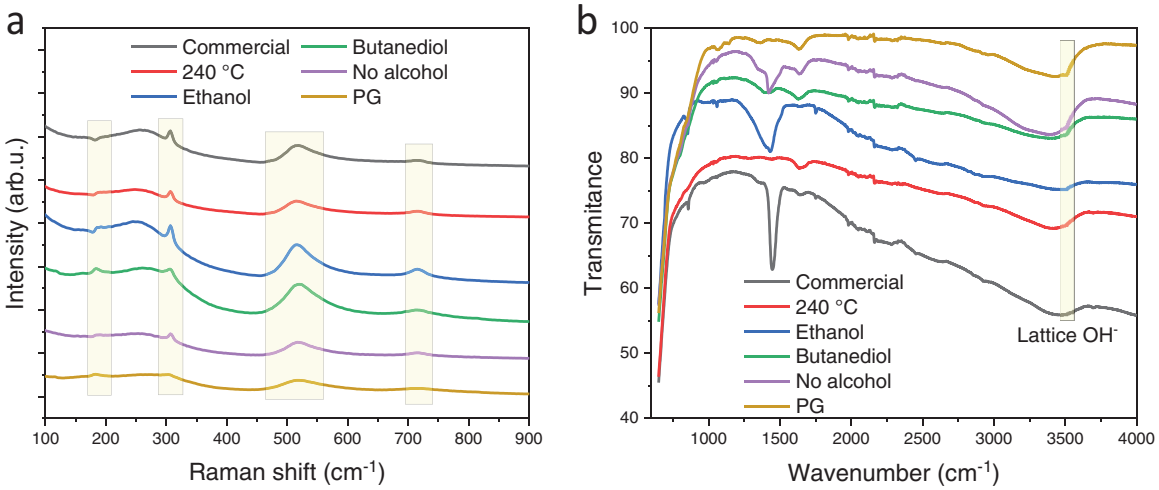

Figure 4. a) Raman spectra of the BTO powders. The bands highlighted in the yellow boxes (185, 310, 515, and 715 cm^{-1}) are originating from the tetragonal structure of BTO. b) FTIR spectra of the BTO samples synthesized under different conditions, and the commercial sample. All the samples were thermally treated for 20 h at 120 °C in order to avoid surface OH^- groups coming from water.

with the higher content of cubic symmetry phase at RT. The commercial sample, with predominance of tetragonal phase, shows no band at this position, implying that the cubic symmetry phase and the presence of lattice OH^- within the crystalline structure are related.

2.4. Strain Analysis from Diffraction Data

In addition to the Rietveld analysis, we used the Williamson–Hall (W–H) approach to determine the inhomogeneous strain and crystallite size for the BTO samples from the XRD data. The W–H plot for the samples BTO PG, butanediol, and ethanol are shown in Figure 2b. Figure S3, Supporting Information, shows the plot for the other samples. The slope of the peak width versus Q plot is a direct measure of microstrain.[30] One example of the fitting method used to extract the peak widths is shown in Figure S4, and Table S3, Supporting Information, summarizes the results. For the BTO PG and butanediol samples, which are fully cubic, the slope is very strong indicating the presence of inhomogeneous strain.

Another remarkable feature seen in the W–H parameters is that the crystallite size (intercept of W–H plot) for the BTO PG, butanediol and no alcohol samples is smaller than seen in the SEM images (Figure 1). For the 240 °C sample, the crystallite size is 27.7 nm for the cubic phase and 23.7 nm for the tetragonal phase. The same can be seen in the BTO ethanol and no alcohol samples, where the crystallite size is 102 and 45 nm for the tetragonal portion, respectively, while for the cubic portion it is very small (negative intercept). These trends are in accordance with the Rietveld refinement, although the strain values obtained from the Rietveld are slightly larger than from the W–H plots. Given that the strain is more pronounced for larger 2θ angles, this discrepancy is probably due to the fact that the Rietveld refinement was done over a broad range of scattering angles, whereas the W–H plots were made just for the lower angle peaks.

2.5. Bragg Coherent Diffraction Imaging Reconstructions

The Rietveld refinement and the W–H analyses show that microstrain as well as anomalously small grain sizes are associated with the cubic-phase samples. To understand these structural trends, we performed BCDI experiments on individual NPs. This permits the understanding of the strains in terms of real-space images, but has the disadvantage of looking at single particles and lacks the population averaging of the powder diffraction methods. BTO NPs have been imaged before using this technique.[31–33]

Figure 5a–d shows the BCDI reconstructions of the BTO ethanol, PG, butanediol, and 240 °C samples. We measured several nanocrystals from each set of synthesis conditions in our BCDI experiments, and the reconstructions shown here are representative. The sample containing no alcohol did not give a measurable coherent diffraction pattern, indicating the crystallinity was too poor to give a reconstruction. In BCDI, the phase represents the projection of the displacement field on the Q vector direction (black arrows) compared with the atoms in the equilibrium position, as determined by Equation (1):[34]

$$\Phi(r) = Qu(r) \tag{1}$$

where $\Phi(r)$ represents the phase shift measured as a function of position, r, in the image, Q is the momentum transfer vector and $u(r)$ is the displacement vector. Therefore, the positive red colored phase represents atoms displaced in the direction of the Q vector, and the negative blue color is along the opposite direction. From the 3D reconstructions, it can be seen that there are empty electron density regions within the crystals, indicating that any material present is either misoriented or highly strained. In all cases the nanocrystals seen to be divided up into domains with a typical size of ≈50 nm. The transition regions between the domains, whose size is not fully evaluated because of the limited resolution (30 nm), are the domain walls. The phase range for all the reconstructed particles is broad, indicating strong relative displacement of the atoms in

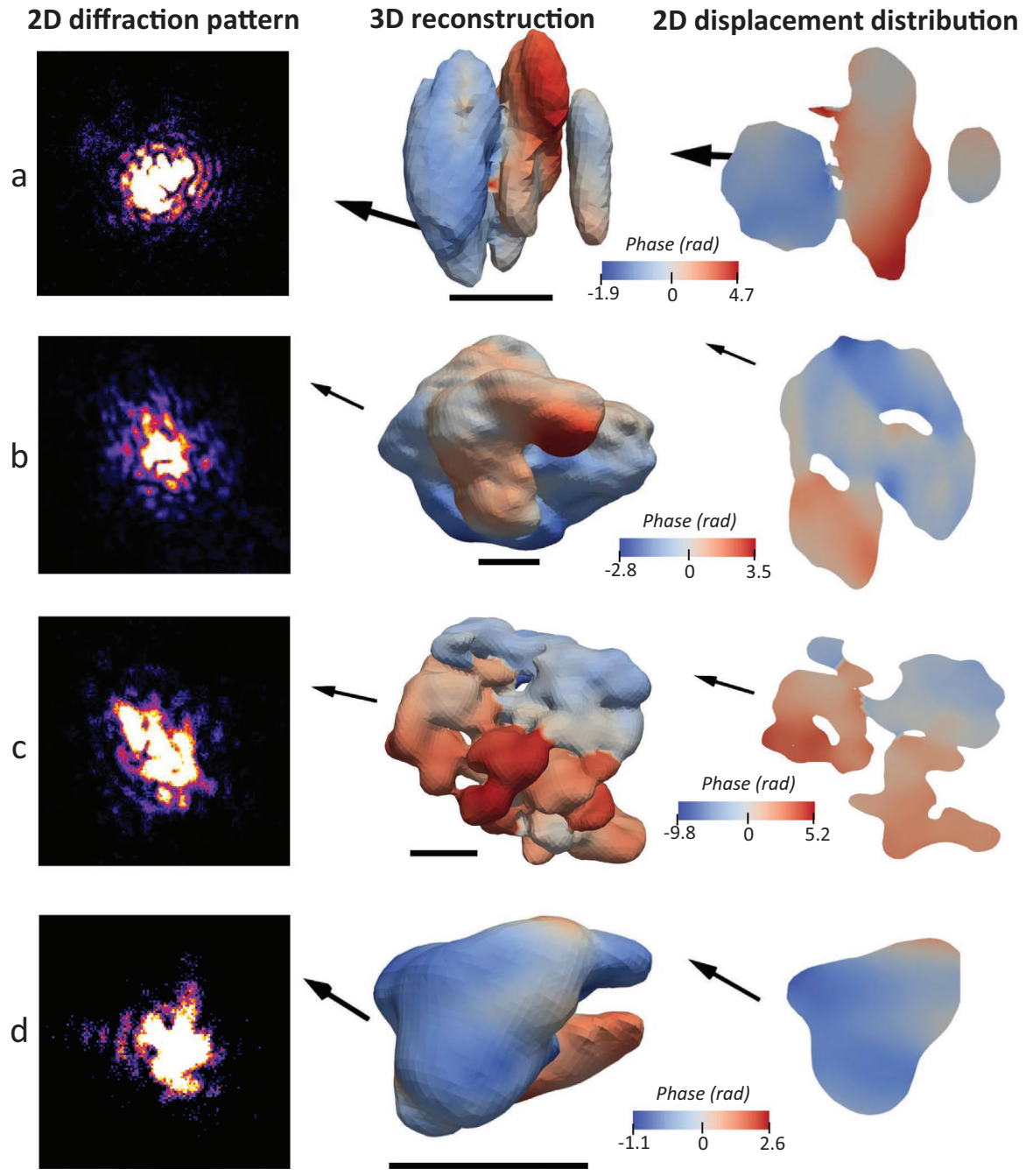

Figure 5. BCDI reconstructions of the BTO nanocrystals synthesized using the hydrothermal approach. First column shows a 2D diffraction pattern close to the center of the recorded rocking curve, the second column the 3D reconstruction of the electron density mapped out as phase, and the third column a cross-section of the phase distribution inside the particle for each sample. a) BTO ethanol; b) BTO PG; c) BTO butanediol and d) BTO 240 °C. The black arrow represents the direction of the Q vector of the (110) reflection. The scale bar represents 100 nm for all the particles.

the crystalline structure, in the same samples that show the pronounced inhomogeneous strain extracted from the Rietveld refinement and W–H plots. Since the structure has significant strain and this is attributed to the domain-wall regions in the simplest picture, these must represent a significant fraction of the total volume.

Figure 6a shows further detail of the 3D reconstruction of one NP measured in our BDCI experiment of the sample BTO 240 °C. Figure 6b shows the 3D reconstruction with a low level of opacity, and the position of one cross sectional slice, which is displayed in Figure 6c. Figure 6d shows the phase line plot over the white line shown in Figure 6c. This triangular phase profile can be explained by the formation of merohedral twins between tetragonal subdomains illustrated in Figure 6e. These twins have interchanged a and c axis directions, which meet at {110} domain walls oriented at ≈45°. The merohedral twin

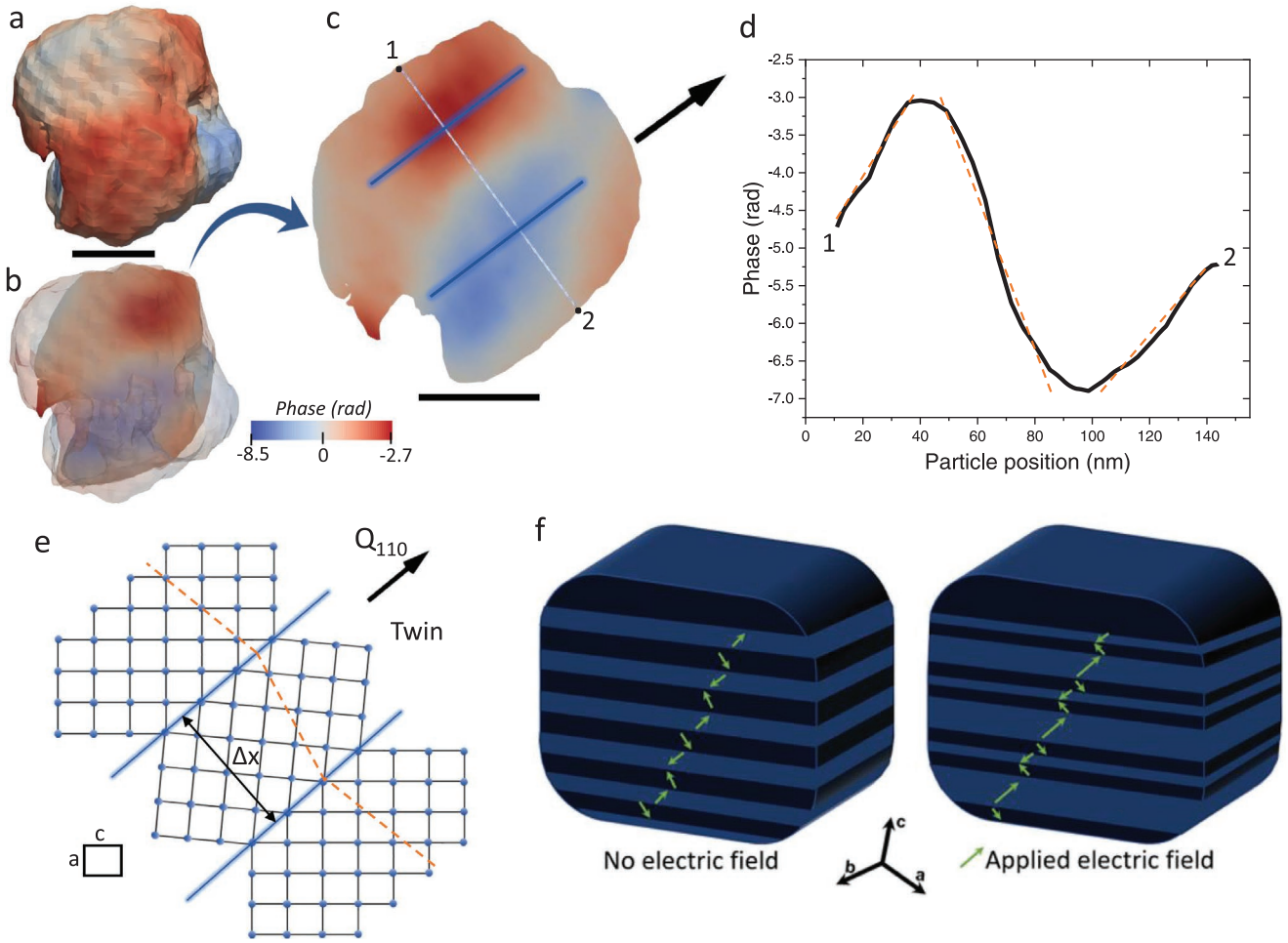

Figure 6. Proposed twin domain model from the BCDI analysis. a) 3D reconstruction of one nanocrystal measured of the sample BTO 240 °C mapped out as a phase isosurface; b) translucent copy showing the position of the cross sectional slice shown in (c); d) phase line plot along the white line shown in (c); points 1 and 2 represent the initial and final points as shown in (c). The phase scale is the same for panels (a–c). e) schematic of a twin domain (central portion of the crystal); the *c*–*a* difference is exaggerated ten times for illustration purposes and the crystalline unit cell is shown on the bottom left, with the lattice parameters c and a. The shaded blue lines represent the merohedral twin boundaries. The orange dashed line in (d) and (e) represent the modulations caused by the presence of the twin, having a distinctive slope. f) Schematic model of the dielectric response: the stripes represent the domains within the NP, and the green arrows represent the direction of the polarization, along the c-axis. The black arrows shown in (c) and (e) represent the direction of the (110) Q vector. The scale bars in (a–c) represent 50 nm; (a) and (b) share the same scale bar.

gives rise to very small-angle grain boundaries, unlike the macroscopic {111} stacking faults reported previously.[35] Considering a twin domain represented in the central portion of the crystalline structure drawn in Figure 6e, it is possible to calculate the shift in phase as a function of the twin spacing distance x (shown in Figure 6e, perpendicular to the Q vector) inside the nanocrystal, based on simple geometric considerations. Quantitative analysis of Figure 6d shows there is a phase shift of 7.36 radians across a twin domain of thickness $\Delta x = 47$ nm; the geometric calculation finds the c/a ratio is 1.0035. This picture is in good agreement with the high strain seen in the Rietveld/W–H plots and with the local tetragonal structure seen by Raman and PDF, as discussed above. Given that the structure is locally tetragonal, if the domains are regularly distributed in the three crystalline directions, the structure would appear cubic on average, which is also consistent with the XRD results. However, since we can see the tetragonal phase in the Rietveld analysis (i.e., long-range order), the distribution of the twin domains is not homogeneous over all the samples.

To explain the enhanced dielectric behavior of nano-sized BTO, we propose a model based on the BCDI result that the cubic state is a superposition of strained tetragonal domains. The model, shown in Figure 6f, is adapted from the conclusions of a field-dependent XRD study[11] and is consistent with our XRD data, Rietveld refinement, PDF analysis, BCDI results, and Raman spectroscopy. When no electric field is applied, the locally tetragonal domains are present in the three different crystallographic directions in the sample, cancelling out the polarization. When an external electric field is applied, the domains pointing in the field direction tend to get bigger, giving rise to a net polarization. Because the 90° twin boundaries are free of defects, they can migrate rapidly and provide the high-frequency performance needed for the MLCCs. The presence of 90° domain walls in BTO crystals of different sizes

and synthesized under different conditions was described before.[11,14,36] However, these previous works did not make the connection between the presence of the cubic phase and the size-dependent dielectric properties of BTO.

Oxygen vacancies are a common defect in oxide perovskite structures, and it is highly important for perovskite-based technologies. Although the presence of oxygen vacancies can at some level contribute to the displacement distribution seen here, the presence of domains seen in our BCDI analysis cannot be due to this type of point defect. If this were the case, we would have domain regions rich in oxygen vacancies, and others poor in oxygen vacancies, which is very unlikely. Raman spectra (Figure 4a) also contribute to this conclusion. Zhang and co-workers[37] studied BTO samples prepared under different annealing/environmental conditions and compared them with a pristine sample. They reported the appearance of a broad band in the region 200–250 cm^{-1} and attributed that to the oxygen vacancies generated in the surface of one of the heat-treated samples. In our case, we do not detect the presence of this band.

BCDI reconstructions for the BTO commercial sample are discussed elsewhere.[32] The hydrothermally synthesized BTO NPs reported here, have a much higher level of disorder. The locally tetragonal domains we find in the long-range cubic nanoparticles are so small that the diffraction patterns overlap completely within a single broadened Bragg peak. The coherent diffraction experiment can decode the strong interference between the domains and allows their relative locations and phases to be determined uniquely.

3. Conclusions

In summary, BTO nanoparticles were prepared by hydrothermal synthesis. While Raman spectroscopy and PDF analysis revealed that the crystalline structure is locally tetragonal, XRD analysis showed the presence of mixtures of tetragonal and cubic phases, with more cubic phase appearing at lower synthesis temperatures, in agreement with previous reports. Rietveld refinement and the W–H analysis show the presence of a significant microstrain, as well as anomalously small particle sizes in the metastable cubic phase. BCDI was then used to image the synthesized nanoparticles. BCDI results show a significant presence of ≈50 nm sub-domains within the nanoparticles with significant variations of the image phase, interpreted as lattice displacements. We rationalize these results with a model containing merohedral twin domains within the nanocrystals, which differs from previously considered explanations of the stabilization of the cubic phase at room temperature, even though it is not thermodynamically favored. The conclusion is that the structure is locally tetragonal, made up of twin domains with the c-axis pointing in different directions; the average structure tends to be cubic. Finally, we propose a model where the domain sizes can adjust by facile migration of twin domain walls to enlarge those domains oriented in the direction of an electric field, leading to an enhanced dielectric response. Our work neatly explains why the previous parallel observations of cubic structure and dielectric anomalies for nano-sized BTO appear to coincide. It demonstrates the importance of complementary structural characterization to explain the commercially important observation that ≈100 nm sized crystals have a significantly higher dielectric constant.[38]

4. Experimental Section

Barium Titanate Crystals Synthesis at 180 °C: The synthesis protocol adopted in this work was based on ref. [39]. In brief, 0.133 mL of $TiCl_4$ was added dropwise into a solution containing 12.5 mL of deionized water and 1 g of different alcohols (ethanol, propylene glycol, butanediol) was added in a 50 mL two-neck round-bottom flask. As the hydrolysis and condensation reaction of the Ti precursor is extremely exothermic, the procedure was done in an ice bath container. After 20 min stirring, 15 mL of a 3 M LiOH solution was added in the case of the sample prepared with ethanol, and a solution containing 10 g of KOH in 15 mL of deionized water was added in the case of the propylene glycol/butanediol samples. After 5 min stirring, 5 mL of a 0.2815 M $BaCl_2.2H_2O$ solution was added, followed by 5 min of stirring. The resulting solution was transferred to a 100 mL Teflon-lined stainless-steel autoclave, that was maintained for 48 h at 180 °C. The resulting powder was centrifuged and washed several times with deionized water and ethanol and left to dry overnight at 70 °C. Finally, the sample "no alcohol" was synthesized with no alcohol source in the synthesis route. The Ba/Ti molar ratio was 1.16 for this set of samples. The samples were named with the respective alcohol used in the synthesis procedure, or with "no alcohol" when it was not used. The sample made with propylene glycol was named as BTO-PG.

Barium Titanate Crystals Synthesis at 240 °C: In an attempt to synthesize BTO in the tetragonal phase, the major adjustment done was the higher temperature (240 °C). Following the protocol proposed by Huarui et al.,[21] the Ba/Ti molar ratio was also increased to 1.6. In a typical synthesis, 1.37 mL of $TiCl_4$ was added into 20 mL of deionized water contained in a 50 mL 2 neck round bottom flask. The flask was maintained in a cooled ice bath recipient, and the system was left under stirring for 20 min. Then, 20 mL of a 1 M $BaCl_2.2H_2O$ solution was added, followed by 20 min of stirring. Then, a solution containing 4 g of NaOH in 10 mL of deionized water was added and the system was left under stirring for 5 min. This sample was named 240 °C.

BTO Commercial Sample: A commercial BTO sample (200 nm nominal particle size) was purchased from Santa Cruz Biotechnology. The CAS (Chemical Abstracts Service) registry number for the commercial sample is 12047-27-7.

Scanning Electron Microscopy: The SEM imaging was performed using a Hitachi 4800 microscope operating in an accelerating voltage of 5 kV at Center of Functional Nanomaterials (CFN) at Brookhaven National Laboratory (BNL). The sample was prepared by drop-casting ≈10 µg of the BTO powders dispersed in ethanol on Si wafer, which was left to dry at RT prior to analysis.

Synchrotron X-Ray Diffraction: The crystalline structure of the samples was investigated by synchrotron XRD in two different beamlines: 11-BM at Advanced Photon Source (APS) using a wavelength of 0.457895 Å and at 7-BM beamline at National Synchrotron Light Source II (NSLS-II) in two different experiments, using a source wavelength of 0.62166 Å in one of them, and 0.49594 Å in the other. All the synchrotron XRD experiments were done in a Debye–Scherrer geometry (transmission). Crystalline phases were identified, and the structure was refined by the Rietveld method using the software TOPAS. The W–H plots were done using the Lorentzian Function for the commercial sample, and Pseudo–Voigt Function for the other samples to fit the Bragg peaks. From the fits, the 2θ position, the FWHM, β, and the error were extracted, for preparing the subsequent $\beta\cos(\theta)$ versus $4\sin(\theta)$ plot. The plots were then linearly fitted, and the vertical error bars were included in the plots. For the ethanol sample, which had a large amount of barium carbonate, when its peak positions were coincident with the BTO, the peak was not used in the W–H plot.

Raman Spectroscopy: Raman spectroscopy was done under ambient pressure, with a laser wavelength of 532 nm in a backscattering geometry. The Raman spectrometer consisted of a Thermo Scientific DXR Raman Microscope, using a 20× objective lens with 10 mW power setting. The stability of the sample was tested under this laser power, after tests were done on a range of laser powers (3 to 10 mW), and the sample was found to be stable.

Fourier Transform Infrared Spectroscopy: FTIR was performed in a PerkinElmer instrument Spectrum 100 FTIR Spectrometer at RT in the wavenumber range 650–4000 cm^{-1}. The powder was compressed in the equipment and measured in the attenuated total reflection (ATR) mode.

Synchrotron X-Ray Atomic Pair Distribution Function (PDF) Measurements: Room temperature X-ray total scattering data were collected at 28-ID-1 beamline of the NSLS II at Brookhaven National Laboratory. Powder samples of $BaTiO_3$ were sealed in 1 mm (outer diameter) polyimide capillary. Measurements were carried out in transmission geometry using a 2D PerkinElmer amorphous silicon area detector (2048 × 2048 pixels with 200 μm^2 pixel size) placed ≈204 mm downstream of the sample. The setup utilized a monochromatic X-ray beam with 74.5 keV energy ($\lambda = 0.1665$ Å). The X-ray diffraction data were converted to PDFs using pyFAI and PDFgetX3 software.

PDF Data Processing and Analysis: Calibrations of the experimental geometry, momentum transfer (Q) range, and detector orientation were carried out by utilizing nickel standard measurements performed under the same conditions. Appropriate masking of the beam-stop shadow, inactive and outlier pixels, and subsequent azimuthal integration of the 2D images to obtain 1D diffraction patterns of intensity versus Q data were done using pyFAI software package.[40,41] Standardized corrections to the data for experimental effects to obtain the reduced total scattering structure function, $F(Q)$, and the subsequent sine Fourier transforms to obtain experimental PDFs, $G(r)$, with $Q_{max} = 25$ $Å^{-1}$ were carried out using the PDFgetX3 program within the xPDFsuite software package.[42] The PDF analysis was carried out using the PDFgui[43] modeling platform.

Bragg Coherent Diffraction Imaging: BCDI was performed at the 34-ID-C beamline at APS in parallel experiments, done at RT. The coherent X-ray beam was produced by an undulator on this 3rd generation synchrotron. The coherent flux at this beamline is 10^9 photons per s. A double crystal monochromator selected the energy to 9 or 10 keV, depending on the experiment, and Kirkpatrick–Baez (KB) mirrors were used to focus the beam to 600 × 600 nm^2 size. A Medipix detector (512 × 512 pixels 55 × 55 μm^2) was placed on the (110) reflection of BTO, and the 2D coherent diffraction patterns were recorded in rocking curve scans by rotating the Bragg angle using small angle intervals. The Bragg angle was rotated +/− 0.4° collecting 80 points, or +/− 0.8° collecting 160 points, depending on the sample. The exposure time varied between 4–8 s depending on the sample. The detector was placed 0.5–1 m from the sample, depending on the experiment. For larger sample to detector distances, the oversampling ratio is larger; however, it must be considered that increasing the distance also leads to a lower signal-to-noise ratio, which affects the reconstruction process. The samples were prepared by drop-casting the powder dispersed in ethanol on Si wafer substrates; then, the top part of the samples was covered with a tetraethyl orthosilicate (TEOS) solution prepared in ethanol; the Si wafer was then placed in a tubular furnace at 300 °C for 3 h for the TEOS condensation reaction and subsequent formation of an SiO_2 rigid network. This is a common procedure when performing BCDI to fix the nanocrystals on the substrate in order to avoid nanoparticle movement caused by the beam interaction.[44]

Reconstruction of the Nanocrystals: A total of 620 iterations were used alternating error reduction (ER) and hybrid-input-output (HIO) algorithms.[45] The phase retrieval code was initiated with 20 ER iterations, followed by 180 iterations of the HIO algorithm, starting from random phases. The 3D reconstructions were plotted as an isosurface of the image amplitude, and also 2D cross-sections using the software Paraview.[46] The images were colored with the recovered phase originated from the mathematical reconstruction. The pixel size of the phase retrieval reconstructions varied in the range 4.11–8.22 nm for the nanoparticles shown in this paper. The final resolution achieved for the reconstruction was determined by line profiles to be 30 nm.

The Williamson–Hall Approach: Inhomogeneous strain is well known to cause systematic broadening of powder diffraction peaks. For example, if the crystalline structure was both contracted and expanded, the Bragg peaks would become broadened toward both sides. The second common source of broadening was the finite size effect: smaller crystals gave broader peaks. One could calculate the crystallite size using the well-known Scherrer formula,[47] taking into account the full width at half maximum (FWHM) of the Bragg peaks. When the both sources of broadness were combined, one could separate the size and the inhomogeneous strain contributions in a straightforward way using the W–H approach,[30] by expressing the peak width as the sum of two terms:

$$\beta_{tot} = C\varepsilon \tan\theta + \frac{K\lambda}{L\cos\theta} \quad (2)$$

where β_{tot} is the total broadness coming from both inhomogeneous strain and the crystallite size, C and K are constants, ε is the inhomogeneous strain, θ is the Bragg angle, λ is the wavelength of the radiation, and L is the particle size. If both sides of the equation were multiplied by $\cos\theta$ a linear equation was obtained, which was the W–H plot. From the plot of $\beta_{tot}\cos\theta$ versus $\sin\theta$ one could obtain the inhomogeneous strain component from the slope, $C\varepsilon$, and the crystallite size from the intercept, $\frac{K\lambda}{L}$.

Supporting Information

Supporting Information is available from the Wiley Online Library or from the author.

Acknowledgements

One of the XRD measurements (beamline 11-BM) and the BDCI experiment (beamline 34-ID-C) was carried out at the Advanced Photon Source, a U.S. DOE Office of Science User Facility operated for the DOE Office of Science by Argonne National Laboratory under Contract No. DE-AC02-06CH11357. Additional XRD measurements took place at the 7-BM (QAS) beamline, while the PDF measurements were made at the 28-ID-1 (PDF) beamline of the National Synchrotron Light Source II (NSLS-II). Synthesis and data analysis were supported by the DOE Office of Science by Brookhaven National Laboratory under Contract No. DESC0012704. The NSLS-II and the Center for Functional Nanomaterials, used for SEM characterization, are U.S. DOE Office of Science User Facilities operated for the DOE Office of Science by Brookhaven National Laboratory under Contract No. DESC0012704. Work performed at UCL was supported by EPSRC. For the purpose of open access, the author has applied a Creative Commons Attribution (CC BY) license to any Author Accepted Manuscript version arising.

Conflict of Interest

The authors declare no conflict of interest.

Data Availability Statement

The data that support the findings of this study are available from the corresponding author upon reasonable request.

Keywords

90° domain walls, barium titanate, Bragg coherent diffraction imaging, dielectric enhancement, nanoparticles

Received: July 13, 2022
Revised: December 1, 2022
Published online:

[1] G. H. Kwei, A. C. Lawson, S. J. L. Billinge, S. W. Cheong, *J. Phys. Chem.* **1993**, *97*, 2368.
[2] C. H. Ahn, K. M. Rabe, J.-M. Triscone, *Science* **2004**, *303*, 488.
[3] A. R. Damodaran, J. C. Agar, S. Pandya, Z. Chen, L. Dedon, R. Xu, B. Apgar, S. Saremi, L. W. Martin, *J. Phys. Condens. Matter* **2016**, *28*, 263001.
[4] H. Thurnauer, J. Deaderick, U.S. Patent No. 2429588 **1947**.
[5] L. Curecheriu, M. T. Buscaglia, V. Buscaglia, Z. Zhao, L. Mitoseriu, *Appl. Phys. Lett.* **2010**, *97*, 242909.
[6] S. A. Patil, D. V. Shinde, D.o Y. Ahn, D. V. Patil, K. K. Tehare, V. V. Jadhav, J. K. Lee, R. S. Mane, N. K. Shrestha, S.-H. Han, *J. Mater. Chem. A* **2014**, *2*, 13519.
[7] M. Parashar, V. K. Shukla, R. Singh, *J. Mater. Sci.* **2020**, *31*, 3729.
[8] S. Brahma, C.-P.u Liu, S. A. Shivashankar, *J. Phys. D Appl. Phys.* **2017**, *50*, 0.
[9] T. Hoshina, *J. Ceram. Soc. Jpn.* **2013**, *121*, 156.
[10] T. Hoshina, S. Wada, Y. Kuroiwa, T. Tsurumi, *Appl. Phys. Lett.* **2008**, *93*, 2006.
[11] D. Ghosh, A. Sakata, J. Carter, P. A. Thomas, H. Han, J. C. Nino, J. L. Jones, *Adv. Funct. Mater.* **2014**, *24*, 885.
[12] L. E. Cross, A. J. Moulson, *Ferroelectrics* **1984**, *54*, 147.
[13] W. R. Buessem, L. E. Cross, A. K. Goswami, *J. Am. Ceram. Soc.* **1966**, *49*, 33.
[14] G. Arlt, D. Hennings, G. De With, *J. Appl. Phys.* **1985**, *58*, 1619.
[15] X. Zhu, J. Wang, Z. Zhang, J. Zhu, S. Zhou, Z. Liu, N. Ming, *J. Am. Ceram. Soc.* **2008**, *91*, 1002.
[16] D. Chen, X. Jiao, *J. Am. Ceram. Soc.* **2000**, *83*, 3.
[17] L. R. Prado, N. S. De Resende, R. S. Silva, S. M. S. Egues, G. R. Salazar-Banda, *Chem. Eng. Process. Process Intensif.* **2016**, *103*, 12.
[18] M. Boulos, S. Guillemetfritsch, F. Mathieu, B. Durand, T. Lebey, V. Bley, *Solid State Ionics* **2005**, *176*, 1301.
[19] R. Vivekanandan, T. R. N. Kutty, *Powder Technol.* **1989**, *57*, 181.
[20] I. J. Clark, T. Takeuchi, N. Ohtori, D. C. Sinclair, *J. Mater. Chem.* **1999**, *9*, 83.
[21] H. Xu, L. Gao, J. Guo, *J. Eur. Ceram. Soc.* **2002**, *22*, 1163.
[22] R. Asiaie, W. Zhu, S. A. Akbar, P. K. Dutta, *Chem. Mater.* **1996**, *8*, 226.
[23] M. H. Frey, D. A. Payne, *Phys. Rev. B Condens. Matter Mater. Phys.* **1996**, *54*, 3158.
[24] H. Zhang, J. F. Banfield, *J. Mater. Chem.* **1998**, *8*, 2073.
[25] K. Page, T. Proffen, M. Niederberger, R. Seshadri, *Chem. Mater.* **2010**, *22*, 4386.
[26] M. S. Senn, D. A. Keen, T. C. A. Lucas, J. A. Hriljac, A. L. Goodwin, *Phys. Rev. Lett.* **2016**, *116*, 207602.
[27] U. D. Venkateswaran, V. M. Naik, R. Naik, *Phys. Rev. B* **1998**, *58*, 14256.
[28] M. P. Fontana, M. Lambert, *Solid State Commun.* **1972**, *10*, 1.
[29] F. A. Rabuffetti, R. L. Brutchey, *J. Am. Chem. Soc.* **2012**, *134*, 9475.
[30] G. K. Williamson, W. H. Hall, *Acta Metall.* **1953**, *1*, 22.
[31] D. Karpov, Z. Liu, T. D. S. Rolo, R. Harder, P. V. Balachandran, D. Xue, T. Lookman, E. Fohtung, *Nat. Commun.* **2017**, *8*, 280.
[32] J. Diao, X. Shi, T. A. Assefa, L. Wu, A. F. Suzana, D. S. Nunes, D. Batey, S. Cipiccia, C. Rau, R. J. Harder, W. Cha, I. K. Robinson, *Phys. Rev. Mater.* **2020**, *4*, 106001.
[33] N. Oshime, K. Ohwada, A. Machida, N. Fukushima, S. Ueno, I. Fujii, S. Wada, K. Sugawara, A. Shimada, T. Ueno, T. Watanuki, K. Ishii, H. Toyokawa, K. Momma, S. Kim, S. Tsukada, Y. Kuroiwa, *Jpn. J. Appl. Phys.* **2022**, *61*, SN1008.
[34] I. Robinson, *J. Phys. Soc. Jpn.* **2013**, *82*, 021012.
[35] E. Hamada, W.-S. Cho, K. Takayanagi, *Philos. Mag. A* **1998**, *77*, 1301.
[36] Z.-Y. Shen, J.-F. Li, *J. Ceram. Soc. Jpn.* **2010**, *118*, 940.
[37] W. H. Zhang, L. Chen, Y. T. Tao, W. H. Zhang, J. Chen, J. X. Zhang, *Phys. B Condens. Matter* **2011**, *406*, 4630.
[38] T. Hoshina, H. Kakemoto, T. Tsurumi, S. Wada, M. Yashima, *J. Appl. Phys.* **2006**, *99*, 054311.
[39] L. Dong, H. Shi, K. Cheng, Q.i Wang, W. Weng, W. Han, *Nano Res.* **2014**, *7*, 1311.
[40] G. Ashiotis, A. Deschildre, Z. Nawaz, J. P. Wright, D. Karkoulis, F. E. Picca, J. Kieffer, *J. Appl. Crystallogr.* **2015**, *48*, 510.
[41] J. Kieffer, V. Valls, N. Blanc, C. Hennig, *J. Synchrotron. Radiat.* **2020**, *27*, 558.
[42] P. Juhás, T. Davis, C. L. Farrow, S. J. L. Billinge, *J. Appl. Crystallogr.* **2013**, *46*, 560.
[43] C. L. Farrow, P. Juhas, J. W. Liu, D. Bryndin, E. S. Božin, J. Bloch, T.h Proffen, S. J. L. Billinge, *J. Phys. Condens. Matter* **2007**, *19*, 335219.
[44] M. Monteforte, A. K. Estandarte, B.o Chen, R. Harder, M. H. Huang, I. K. Robinson, *J. Synchrotron. Radiat.* **2016**, *23*, 953.
[45] R. W. Gerchberg, W. O. Saxton, *Optik* **1972**, *35*, 237.
[46] J. Ahrens, B. Geveci, C. Law, in *Visualization Handbook*, Elsevier, Los Alamos National Laboratory, CA, USA **2005**.
[47] A. L. Patterson, *Phys. Rev.* **1939**, *56*, 978.